

Pressure-tuned intralayer exchange in superlattice-like $\text{MnBi}_2\text{Te}_4/(\text{Bi}_2\text{Te}_3)_n$ topological insulators

Jifeng Shao^{1#}, Yuntian Liu^{1#}, Meng Zeng¹, Jingyuan Li¹, Xiao-Ming Ma¹, Feng Jin², Ruie Lu¹,
Yichen Sun¹, Mingqiang Gu¹, Wenbin Wu², Liusuo Wu¹, Chang Liu¹, Qihang Liu^{1,3,4*}, and
Yue Zhao^{1*}

¹Shenzhen Institute for Quantum Science and Engineering and Department of Physics, Southern
University of Science and Technology, Shenzhen 518055, China

²Hefei National Laboratory for Physical Sciences at Microscale, University of Science and
Technology of China, Hefei 230026, China

³Guangdong Provincial Key Laboratory for Computational Science and Material Design,
Southern University of Science and Technology, Shenzhen 518055, China

⁴Shenzhen Key Laboratory of for Advanced Quantum Functional Materials and Devices,
Southern University of Science and Technology, Shenzhen 518055, China

These authors contribute equally to this work.

*To whom correspondence should be addressed: zhaoy@sustech.edu.cn, liuqh@sustech.edu.cn.

Abstract

The magnetic structures of the intrinsic magnetic topological insulator family $\text{MnBi}_2\text{Te}_4(\text{Bi}_2\text{Te}_3)_n$ ($n = 0, 1, 2$) adopt A-type antiferromagnetic (AFM) configurations with ferromagnetic (FM) MnBi_2Te_4 layers stacking through van der Waals interactions. While the interlayer coupling could be effectively tuned by the number of Bi_2Te_3 spacer layers n , the intralayer FM exchange coupling is considered too robust to control. Here, by applying hydrostatic pressure up to 3.5 GPa as an external knob, we discover the opposite responses of magnetic properties for $\text{MnBi}_2\text{Te}_4(\text{Bi}_2\text{Te}_3)_n$ with $n = 1$ and 2. In MnBi_4Te_7 , the Néel temperature decreases with an increasing saturation field as pressure increases, indicating an enhanced interlayer AFM coupling. In sharp contrast, both the magnetic susceptibility and magneto-transport measurements show that $\text{MnBi}_6\text{Te}_{10}$ experiences a phase transition from A-type AFM to quasi two-dimensional FM state with a suppressed saturation field under pressure. First-principles calculations reveal the essential role of the intralayer exchange coupling, which contains the competition between the AFM-preferred direct exchange and FM-preferred superexchange coupling, in determining these magnetic properties. Such a magnetic phase transition is also observed in Sb-doped $\text{MnBi}_6\text{Te}_{10}$ due to similar mechanism, where the in-plane lattice constant is effectively reduced.

In magnetic topological insulators (MTI), the interplay between magnetic order in real space and the topological electronic structure in momentum space gives rise to many novel topological matters and emergent quantum phenomena, such as Weyl fermions, quantum anomalous Hall effect (QAHE), axion insulator phase and chiral Majorana modes[1-6]. A prototypical example is the layered intrinsic MTI MnBi_2Te_4 with the local moments of Mn atoms ferromagnetic (FM) aligned within one layer while adopting an A-type antiferromagnetic (AFM) order along the stacking direction[7-11]. By manipulating the magnetic order in few-layer MnBi_2Te_4 using film thickness and magnetic field, various topological phases have been experimentally realized, including zero-field QAHE and tunable axion insulator and other high order Chern insulator phases[12-17].

In the family of $\text{MnBi}_2\text{Te}_4(\text{Bi}_2\text{Te}_3)_n$, the interplay of magnetism and topology can be further enriched by inserting n layers of non-magnetic topological insulator (TI) Bi_2Te_3 into the van der Waals layered MTI MnBi_2Te_4 [18-29]. Such heterostructure engineering of the non-magnetic TI and MTI building blocks not only reveals termination-dependent surface states and hybridization between different building blocks[25], but also effectively tunes the interlayer exchange coupling between the neighboring magnetic layers, leading to new topological phases associated with different magnetic phases[18, 22, 23, 26]. For $n = 1$, the transport study of MnBi_4Te_7 shows A-type AFM right below Néel temperature and a competing magnetic order of FM state at even lower temperature ($T \sim 1\text{K}$)[20]. As n goes to 2, with a further weakened interlayer coupling between the magnetic layers, both AFM and FM ground states have been reported experimentally[19, 29-31]. Such complex magnetic behaviors could be associated with the competition between the weak interlayer exchange coupling and other magnetic interactions[20, 23]. Despite the complicated magnetism, a two-dimensional (2D) magnet is proposed to dominate the magnetic properties at

large n ($n \geq 3$) with a vanishing interlayer coupling[23, 26]. On the other hand, the intralayer exchange coupling is typically considered as robust FM, and thus difficult to manipulate by experimentally accessible “knobs”.

As a clean, non-intrusive, reversible, and continuous structure tuning technique, hydrostatic pressure is usually utilized to modify the interlayer coupling strength by adjusting the interlayer separation in van der Waals structures[32, 33]. In this work, by applying hydrostatic pressure up to 3.5 GPa, we found in $\text{MnBi}_2\text{Te}_4(\text{Bi}_2\text{Te}_3)_n$ ($n = 1$ and 2) distinct evolution of magnetic properties originated from the manipulation of intralayer exchange coupling. In contrast to the increasing saturation field in MnBi_4Te_7 ($n = 1$), the saturation field of $\text{MnBi}_6\text{Te}_{10}$ ($n = 2$) decreases by half to about 0.1 T at high pressure. In particular, a pure FM-like hysteresis of anomalous Hall resistivity and magnetic susceptibility emerges at 1.98 GPa, where the kinks associated with AFM state vanish completely, suggesting the formation of FM domains. Our first-principles calculation shows that although the interlayer AFM exchange coupling increases with pressure for both $n = 1$ and 2 , hydrostatic pressure also evokes the intralayer competition between the AFM-preferred direct exchange and FM-preferred superexchange coupling within the MnBi_2Te_4 layer. Considering the nearly vanishing interlayer coupling in $\text{MnBi}_6\text{Te}_{10}$ (one order less compared with that of MnBi_4Te_7), the weakening of the intralayer FM exchange coupling will enhance the effect of fluctuation, including magnetic domains, thermal fluctuation, and other magnetic perturbations. As a result, the formation of 2D FM domains reduces the saturation magnetic moment. A similar FM state is also observed in Sb-doped $\text{MnBi}_6\text{Te}_{10}$ with reduced in-plane lattice constant, providing additional evidence of the scenario of competing intralayer coupling. Our results first reveal the delicate role of intralayer exchange coupling in the complex magnetic properties in MTI/TI heterostructures with a variable number of non-magnetic layers.

The single crystals were grown by flux method and characterized by XRD, electrical transport, magnetization at ambient pressure. Both MnBi_4Te_7 and $\text{MnBi}_6\text{Te}_{10}$ crystals show A-type AFM ground state with easy axis parallel to c axis. The magneto-transport and magnetic susceptibility measurements under hydrostatic pressure were taken using a self-clamped BeCu piston-cylinder cell that produces a maximum pressure of 3.5 GPa. The pressure inside the cell was calibrated by measuring the superconducting transition temperature of Pb. Magnetic susceptibility under high pressure was measured using a pre-calibrated Hall sensor. The magnetic properties of the crystals at ambient pressure and the measurement details under high pressure are described in the supplemental material.

Fig. 1a and b present the horizontal and Hall resistivity of MnBi_4Te_7 at various pressure at $T = 2$ K. As pressure increases gradually to 3.39 GPa, the saturation field B_s increases from 2.07 to 3.08 KOe, indicating an increased AFM interlayer exchange coupling. Besides, the FM hysteresis near the spin-flip transition is strongly inhibited at higher pressure, showing suppression of the FM signal. On the other hand, as increasing pressure, we observe a monotonic decrease of Néel temperature from 12.7 K to 9 K, directly contrasting to what could be expected at an enhanced AFM interlayer exchange coupling. Note that since hydrostatic pressure simultaneously compresses the in-plane and out-of-plane lattice parameters, the decreased T_N could be related to the intralayer compression. Fig. 1e-g show the pressure-tuned transport behavior of $\text{MnBi}_6\text{Te}_{10}$. At ambient pressure, the weakened kinks around zero moment in the hysteresis loop mark the reduced interlayer AFM exchange coupling in $\text{MnBi}_6\text{Te}_{10}$ as n increases, see Fig. S1 (b). The magnetic phase transition temperature also decreases as increasing pressure, similar to MnBi_4Te_7 . However, as pressure increases, the saturation field of $\text{MnBi}_6\text{Te}_{10}$ gradually decreases from 0.2 T to 0.08 T, as summarized by Fig. 2f. Moreover, a rather pure FM state emerges at a pressure above

1.39 GPa, evidenced by a butterfly-shaped $\rho_{xx}(B)$ and disappeared kinks associated with the AFM states in $\rho_{xy}(B)$. Since no structural phase transitions are expected at a pressure below 6 GPa in Bi_2Te_3 , MnBi_2Te_4 , and MnBi_4Te_7 single crystals[34-36], it is quite counterintuitive that an FM state emerges as the pressure-induced compression along c axis shall strengthen the interlayer AFM exchange coupling.

To confirm the magnetic phase transition in $\text{MnBi}_6\text{Te}_{10}$, we applied direct magnetic susceptibility and magnetization measurements under high pressure using a pre-calibrated Hall sensor. Fig. 2 shows the temperature dependence of the magnetic susceptibility and the magnetization curves of $\text{MnBi}_6\text{Te}_{10}$ under different pressure. The M-T curve shows bifurcation for the zero-field cooling (ZFC) and field cooling (FC) at 100 Oe at ambient pressure (Fig. 2a), which matches well with the M-T curves directly measured by VSM (Fig. S6b). As pressure increases, the ZFC curve changes from a sharp cusp-like shape to a flat dome with increasing FC susceptibility below the magnetic phase transition temperature. The number of peaks in dM/dH curve reduces to 2 under 1.98 GPa, marking the spin flips between up and down states (Fig. 2b). Based on the observations in both the magneto-transport and magnetization measurements, we conclude that a FM phase transition indeed occurs in $\text{MnBi}_6\text{Te}_{10}$ as pressure increases.

The magnetic ground states of the layered $\text{MnBi}_2\text{Te}_4(\text{Bi}_2\text{Te}_3)_n$ compounds are determined by both interlayer and intralayer exchange coupling. While the interlayer coupling is dictated by the superexchange between Mn-3d orbitals in adjacent layers mediated by the p orbitals of Bi and Te atoms in between, the intralayer coupling is determined by the competition between the superexchange and direct exchange, as shown in Fig. 3a. The former is between two adjacent Mn atoms mediated by a Te atom with a calculated Mn-Te-Mn bond angle about 95° . Thus, the superexchange coupling prefers FM state according to the Goodenough-Kanamori-Anderson

(GKA) rule[37, 38]. The latter prefers AFM coupling because the direct FM hopping between Mn atoms is forbidden for Mn^{2+} high-spin state (d^5). Because of the large Mn-Mn distance (4.4 Å), the direct exchange coupling is much smaller than the superexchange. Therefore, the intralayer FM state is dominant in $\text{MnBi}_2\text{Te}_4(\text{Bi}_2\text{Te}_3)_n$.

To understand the different pressure response in MnBi_4Te_7 and $\text{MnBi}_6\text{Te}_{10}$, we perform first-principles calculations based on three magnetic configurations: G-type AFM, A-type AFM, and FM (Fig. 3b). The strength of the interlayer and intralayer coupling can thus be expressed by the total energy difference $E_{\text{FM}} - E_{\text{A-AFM}}$, $E_{\text{G-AFM}} - E_{\text{A-AFM}}$, respectively. Our calculation shows that the hydrostatic pressure causes the lattice shrinking both along and perpendicular to the stacking direction (Fig. S7). However, hydrostatic pressure monotonically increases the strength of interlayer exchange coupling but decreases the strength of intralayer coupling by about 10% (Fig. 3c). The weakened intralayer coupling can be explained by the competition between direct exchange and superexchange. In our calculation, when the pressure increases to 3 GPa, both of the Mn-Te bond length and the distance between Mn atoms decrease by about 2%, while the Mn-Te-Mn bond angles are almost unchanged. Thus, the AFM-preferred direct exchange, which has a higher power of correlation to the distance ($\sim d_{\text{Mn-Mn}}^{-5}$) [39], will increase much more than superexchange, leading to a reduced magnetic transition temperature and saturation moment shown in Fig. 1.

The distinct behavior of magnetic properties for different $\text{MnBi}_2\text{Te}_4(\text{Bi}_2\text{Te}_3)_n$ under pressure can thus be understood by the competing role of interlayer and intralayer exchange coupling for different number of Bi_2Te_3 spacing layers n . For MnBi_4Te_7 ($n = 1$), the interlayer superexchange coupling dominates the overall AFM magnetic properties with robust intralayer FM coupling. Although the compression of lattice from hydrostatic pressure strengthens its AFM interlayer

coupling, the weakened intralayer FM coupling results in a decreased Néel temperature, consistent with our experimental observation (Fig. 1c). As for $\text{MnBi}_6\text{Te}_{10}$ ($n = 2$), however, the interlayer coupling is one order smaller than that of MnBi_4Te_7 . Despite neutron scattering results showing an A-type AFM phase, the FM intralayer coupling tends to dominate the magnetic nature. Hence, the pressure-induced intralayer fluctuations could suppress the weak interlayer AFM coupling, rendering a quasi-2D ferromagnet with domains at higher pressure (Fig. 1g). The saturation field in such a pressure-induced FM phase is comparable to what was observed in the FM axion insulator $\text{MnBi}_8\text{Te}_{13}$ [31, 40].

To further validate our understanding of the competing intralayer exchange coupling, we investigate the magnetic properties of Sb doped $\text{MnBi}_6\text{Te}_{10}$, where the in-plane lattice constant can also be effectively reduced with an almost-unchanged distance between the magnetic layers[41-45]. The Sb doped $\text{MnBi}_6\text{Te}_{10}$ crystals are prepared by replacing the Bi component with a molar ratio 1/4 of Sb to Bi in the original recipe. The actual composition is found to be $\text{Mn}_{0.77}\text{Sb}_{1.46}\text{Bi}_{4.54}\text{Te}_{9.54}$ by EDX, determined from the average of 18 randomly selected spots on three samples. The actual Sb concentration is about 1.2 times of nominal ratio, similar to Sb-doped MnBi_4Te_7 [43]. Powder and single-crystal XRD results (Fig. S8) show a 0.65% contraction of the in-plane lattice constant, while the out-of-plane lattice component stays around $101.985(8)\text{\AA}$ (with a negligible increase of 0.07%). Interestingly, Fig.4a shows a large bifurcation of ZFC and FC curves at a magnetic ordering temperature of 11.3 K, which is similar to the FM behavior of $\text{MnBi}_8\text{Te}_{13}$, but in contrast with the sharp cusp AFM feature of the parent compound[31]. Moreover, the magnetic susceptibility of Sb doped $\text{MnBi}_6\text{Te}_{10}$ is one order larger than that of the parent, see Fig. S1. The magnetization curve also reveals a similar FM loop as observed in the anomalous Hall effect of the parent at 1.98 GPa (Fig. 4b).

The observation of such an FM state in Sb doped $\text{MnBi}_6\text{Te}_{10}$ strongly supports our scenario of the competing intralayer coupling due to reduced Mn-Mn distance, similar to the pressurized case. In reality, the increase of Sb component may also promote Mn^{Sb} anti-site defects. Considering the migration of Mn and other defects, the competition between intralayer and interlayer coupling can be more complicated, leading to complex magnetic phase transitions observed in MnSb_2Te_4 and heavily Sb doped MnBi_4Te_7 [43, 45]. However, in our case, the Sb component is relatively small. Both the FC magnetic susceptibility and the saturation moment are much higher at 2 K, closer to those of the FM $\text{MnBi}_8\text{Te}_{13}$ [31]. The successful realization of FM state in Sb doped $\text{MnBi}_6\text{Te}_{10}$ provides additional evidence that the intralayer coupling plays an important role in the magnetism of weakly coupled magnetic topological insulator heterostructures.

In summary, we have systematically studied the magnetic and magneto-transport properties of $\text{MnBi}_2\text{Te}_4(\text{Bi}_2\text{Te}_3)_n$ for $n = 1$ and 2 under hydrostatic pressure up to 3 GPa. For $n = 1$, the saturation field increases, and the Néel temperature decreases as increasing pressure due to an enhanced interlayer AFM coupling competing with a weakened intralayer FM coupling. For $n = 2$, where the interlayer AFM coupling is extremely weak, pressure inhibits the intralayer FM exchange coupling, resulting in a magnetic phase transition from A-type AFM to a quasi-2D FM states at around 1.5 GPa. Our results show that the intralayer exchange coupling plays a significant role in determining the magnetic properties of $\text{MnBi}_2\text{Te}_4(\text{Bi}_2\text{Te}_3)_n$. The exchange coupling can be delicately tuned by lattice engineering, such as pressure and chemical substitution. We show that an intrinsic FM state can be realized in both pressurized $\text{MnBi}_6\text{Te}_{10}$ and Sb-doped $\text{MnBi}_6\text{Te}_{10}$. Our results shed light on the intriguing magnetism in the family of $\text{MnBi}_2\text{Te}_4(\text{Bi}_2\text{Te}_3)_n$ and open up opportunities for the realization of various topological phases determined by their magnetic phases.

Acknowledgements

The research was supported by the Key-Area Research and Development Program of Guangdong Province (2019B010931001), National Natural Science Foundation of China under project Nos. 11674150, 11804402, U2032218, 11974326, 11804144, 11974157, 11804342, 12074161, National Key R&D Program of China (2019YFA0704900), Guangdong Innovative and Entrepreneurial Research Team Program (2016ZT06D348 and 2017ZT07C062), the Guangdong Provincial Key Laboratory of Computational Science and Material Design (Grant No. 2019B030301001), the Science, Technology, and Innovation Commission of Shenzhen Municipality (JCYJ20160613160524999 and ZDSYS20190902092905285), the Shenzhen Key Laboratory (Grant No. ZDSYS20170303165926217), Grants G02206304 and G02206404, the Highlight Project (No. PHYS-HL-2020-1) of the College of Science of SUSTech, and Hefei Science Center of Chinese Academy of Sciences. First-principles calculations were also supported by Center for Computational Science and Engineering at SUSTech. We thank Junhao Lin for valuable discussions.

References

1. Qi, X.L., T.L. Hughes, and S.C. Zhang, *Topological field theory of time-reversal invariant insulators*. Physical Review B, 2008. **78**(19).
2. Mong, R.S.K., A.M. Essin, and J.E. Moore, *Antiferromagnetic topological insulators*. Physical Review B, 2010. **81**(24).
3. Wan, X., et al., *Topological semimetal and Fermi-arc surface states in the electronic structure of pyrochlore iridates*. Physical Review B, 2011. **83**(20).
4. Chang, C.Z., et al., *Experimental observation of the quantum anomalous Hall effect in a magnetic topological insulator*. Science, 2013. **340**(6129): p. 167-70.
5. Tokura, Y., K. Yasuda, and A. Tsukazaki, *Magnetic topological insulators*. Nature Reviews Physics, 2019. **1**(2): p. 126-143.
6. Wang, D., et al., *Evidence for Majorana bound states in an iron-based superconductor*. Science, 2018. **362**(6412): p. 333–335.
7. Gong, Y., et al., *Experimental Realization of an Intrinsic Magnetic Topological Insulator*. Chinese Physics Letters, 2019. **36**(7).
8. Lee, S.H., et al., *Spin scattering and noncollinear spin structure-induced intrinsic anomalous Hall effect in antiferromagnetic topological insulator $MnBi_2Te_4$* . Physical Review Research, 2019. **1**(1).
9. Otrokov, M.M., et al., *Prediction and observation of an antiferromagnetic topological insulator*. Nature, 2019. **576**(7787): p. 416-422.
10. Yan, J.Q., et al., *Crystal growth and magnetic structure of $MnBi_2Te_4$* . Physical Review Materials, 2019. **3**(6).
11. Sass, P.M., et al., *Magnetic Imaging of Domain Walls in the Antiferromagnetic Topological Insulator $MnBi_2Te_4$* . Nano Letter, 2020. **20**(4): p. 2609-2614.
12. Liu, C., et al., *Robust axion insulator and Chern insulator phases in a two-dimensional antiferromagnetic topological insulator*. Nat. Mater., 2020. **19**(5): p. 522-527.
13. Li, J., et al., *Intrinsic magnetic topological insulators in van der Waals layered $MnBi_2Te_4$ -family materials*. Sci. Adv., 2019. **5**(6): p. eaaw5685.
14. Otrokov, M.M., et al., *Unique Thickness-Dependent Properties of the van der Waals Interlayer Antiferromagnet $MnBi_2Te_4$ Films*. Phys. Rev. Lett., 2019. **122**(10): p. 107202.
15. Zhang, D., et al., *Topological Axion States in the Magnetic Insulator $MnBi_2Te_4$ with the Quantized Magnetoelectric Effect*. Phys. Rev. Lett., 2019. **122**(20): p. 206401.
16. Deng, Y., et al., *Quantum anomalous Hall effect in intrinsic magnetic topological insulator $MnBi_2Te_4$* . Science, 2020. **367**(6480): p. 895-900.
17. Ge, J., et al., *High-Chern-number and high-temperature quantum Hall effect without Landau levels*. National Science Review, 2020. **7**(8): p. 1280-1287.
18. Vidal, R.C., et al., *Topological Electronic Structure and Intrinsic Magnetization in $MnBi_4Te_7$: A Bi_2Te_3 Derivative with a Periodic Mn Sublattice*. Physical Review X, 2019. **9**(4).
19. Shi, M.Z., et al., *Magnetic and transport properties in the magnetic topological insulators $MnBi_2Te_4(Bi_2Te_3)_n$ ($n=1,2$)*. Physical Review B, 2019. **100**(15).
20. Wu, J., et al., *Natural van der Waals heterostructural single crystals with both magnetic and topological properties*. Sci. Adv., 2019. **5**(11): p. eaax9989.

21. Sun, H., et al., *Rational Design Principles of the Quantum Anomalous Hall Effect in Superlatticelike Magnetic Topological Insulators*. Phys. Rev. Lett., 2019. **123**(9): p. 096401.
22. Tan, A., et al., *Metamagnetism of Weakly Coupled Antiferromagnetic Topological Insulators*. Phys. Rev. Lett., 2020. **124**(19): p. 197201.
23. Wu, J., et al., *Toward 2D Magnets in the $(\text{MnBi}_2\text{Te}_4)(\text{Bi}_2\text{Te}_3)_n$ Bulk Crystal*. Adv. Mater., 2020: p. e2001815.
24. Hu, C., et al., *A van der Waals antiferromagnetic topological insulator with weak interlayer magnetic coupling*. Nat. Commun., 2020. **11**(1): p. 97.
25. Wu, X., et al., *Distinct Topological Surface States on the Two Terminations of MnBi_4Te_7* . Physical Review X, 2020. **10**(3).
26. Hu, C., et al., *Realization of an intrinsic ferromagnetic topological state in $\text{MnBi}_8\text{Te}_{13}$* . Sci Adv, 2020. **6**(30): p. eaba4275.
27. Ding, L., et al., *Crystal and magnetic structures of magnetic topological insulators MnBi_2Te_4 and MnBi_4Te_7* . Physical Review B, 2020. **101**(2).
28. Tian, S., et al., *Magnetic topological insulator $\text{MnBi}_6\text{Te}_{10}$ with a zero-field ferromagnetic state and gapped Dirac surface states*. Physical Review B, 2020. **102**(3).
29. Yan, J.Q., et al., *A-type antiferromagnetic order in MnBi_4Te_7 and $\text{MnBi}_6\text{Te}_{10}$ single crystals*. Physical Review Materials, 2020. **4**(5).
30. Tian, S., et al., *Magnetic topological insulator $\text{MnBi}_6\text{Te}_{10}$ with a zero-field ferromagnetic state and gapped Dirac surface states*. Phys. Rev. B, 2020. **102**(3): p. 035144.
31. Hu, C., et al., *Realization of an intrinsic ferromagnetic topological state in $\text{MnBi}_8\text{Te}_{13}$* . Sci. Adv., 2020. **6**(30): p. eaba4275.
32. Li, T., et al., *Pressure-controlled interlayer magnetism in atomically thin CrI_3* . Nat. Mater., 2019. **18**(12): p. 1303-1308.
33. Song, T., et al., *Switching 2D magnetic states via pressure tuning of layer stacking*. Nat. Mater., 2019. **18**(12): p. 1298-1302.
34. Pei, C., et al., *Pressure-Induced Topological and Structural Phase Transitions in an Antiferromagnetic Topological Insulator*. Chinese Physics Letters, 2020. **37**(6).
35. Chen, K.Y., et al., *Suppression of the antiferromagnetic metallic state in the pressurized MnBi_2Te_4 single crystal*. Physical Review Materials, 2019. **3**(9).
36. Zhang, J.L., et al., *Pressure-induced superconductivity in topological parent compound Bi_2Te_3* . Proc. Natl. Acad. Sci. USA, 2011. **108**(1): p. 24-8.
37. Goodenough, J.B., *Theory of the Role of Covalence in the Perovskite-Type Manganites $[\text{La}, \text{M(II)}]\text{MnO}_3$* . Physical Review, 1955. **100**(2): p. 564-573.
38. Anderson, P.W., *New Approach to the Theory of Superexchange Interactions*. Physical Review, 1959. **115**(1): p. 2-13.
39. Li, X. and J. Yang, *CrXTe_3 ($X = \text{Si}, \text{Ge}$) nanosheets: two dimensional intrinsic ferromagnetic semiconductors*. Journal of Materials Chemistry C, 2014. **2**(34).
40. Lu, R., et al., *Half-Magnetic Topological Insulator*. arXiv, 2020.
41. Chen, B., et al., *Intrinsic magnetic topological insulator phases in the Sb doped MnBi_2Te_4 bulks and thin flakes*. Nat. Commun., 2019. **10**(1): p. 4469.
42. Yan, J.Q., et al., *Evolution of structural, magnetic, and transport properties in $\text{MnBi}_{2-x}\text{Sb}_x\text{Te}_4$* . Physical Review B, 2019. **100**(10).

43. Chaowei Hu, Scott Mackey, and a.N. Ni, *Switching on ferromagnetic coupling by Mn/Sb antisite disorder in $Mn(Bi_{1-x}Sb_x)_4Te_7$: from electron-doped antiferromagnet to hole-doped ferrimagnet*. arXiv:2008.09097v1, 2020.
44. Bo Chen, et al., *Coexistence of Ferromagnetism and Topology by Charge Carrier Engineering in intrinsic magnetic topological insulator $MnBi_4Te_7$* . arXiv:2009.00039v1 2020.
45. Yaohua Liu, et al., *Site mixing engineers the magnetism of $MnSb_2Te_4$* . arXiv:2007.12217, 2020.

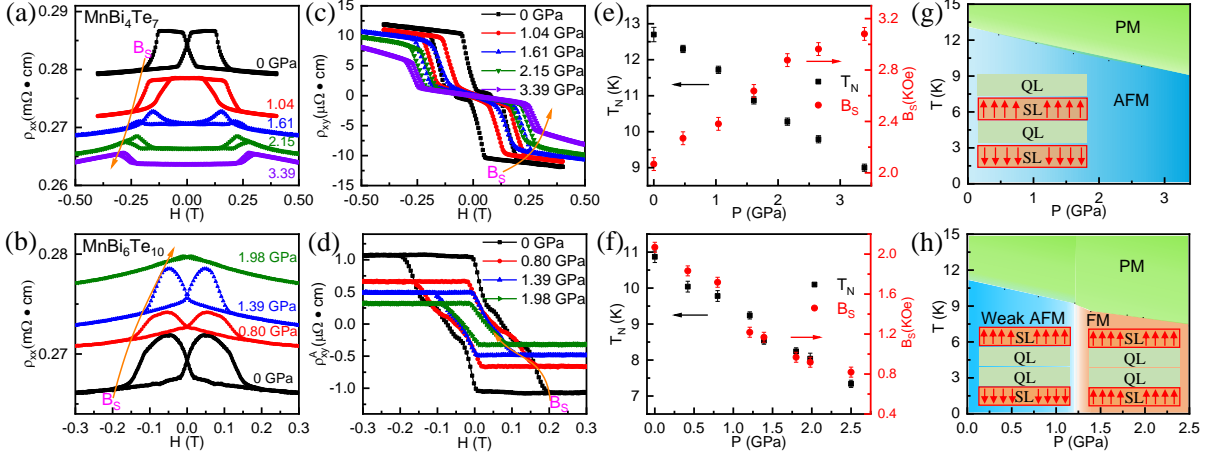


Fig. 1. Pressure tuned magnetism of MnBi_4Te_7 and $\text{MnBi}_6\text{Te}_{10}$. (a-b) Field dependence of the magnetoresistivity ρ_{xx} of MnBi_4Te_7 (a) and $\text{MnBi}_6\text{Te}_{10}$ (b) under different pressure. (c-d) Field dependence of the Hall resistivity ρ_{xx} (or anomalous Hall resistivity ρ_{xy}^A) of MnBi_4Te_7 (c) and $\text{MnBi}_6\text{Te}_{10}$ (d). The orange curved arrows mark the change of saturation field as pressure increases. A pure FM phase occurs for $\text{MnBi}_6\text{Te}_{10}$ at 1.98 GPa. All data were taken at 2 K. The two curves at zero pressure in (a) and (c) are shifted for clarity. The evolution of magnetic phase transition temperature (black square) and saturation field (red dot) with pressure are summarized for MnBi_4Te_7 (e) and $\text{MnBi}_6\text{Te}_{10}$ (f). As increasing pressure, the magnetic ordering temperature decreases for both crystals, while the saturation field responds differently. (g) and (h) are the schematic phase diagrams of MnBi_4Te_7 and $\text{MnBi}_6\text{Te}_{10}$, respectively. SL and QL represent the MnBi_2Te_4 septuple layer and the Bi_2Te_3 quintuple layer.

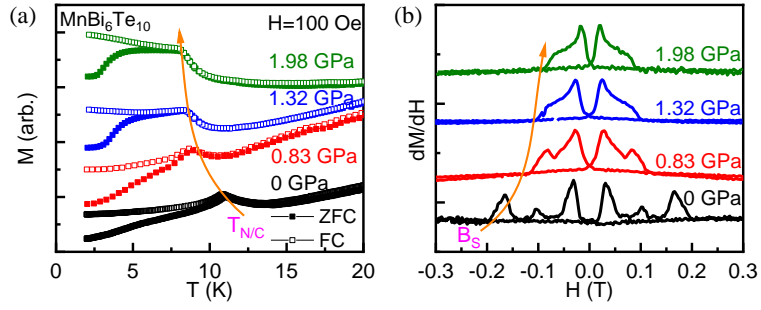


Fig. 2. Magnetic susceptibility measurements of $\text{MnBi}_6\text{Te}_{10}$ under pressure. (a) Temperature dependence of zero-field-cooled (ZFC) and field-cooled (FC) magnetic susceptibility of $\text{MnBi}_6\text{Te}_{10}$ at different pressures under an applied magnetic field of 100 Oe along c axis. (b) Isothermal magnetization of $\text{MnBi}_6\text{Te}_{10}$ at 2 K at various pressure with magnetic field along c axis. The curves are shifted for clarify. The orange curved arrows mark the evolution of magnetic ordering temperature and saturation field as increasing pressure.

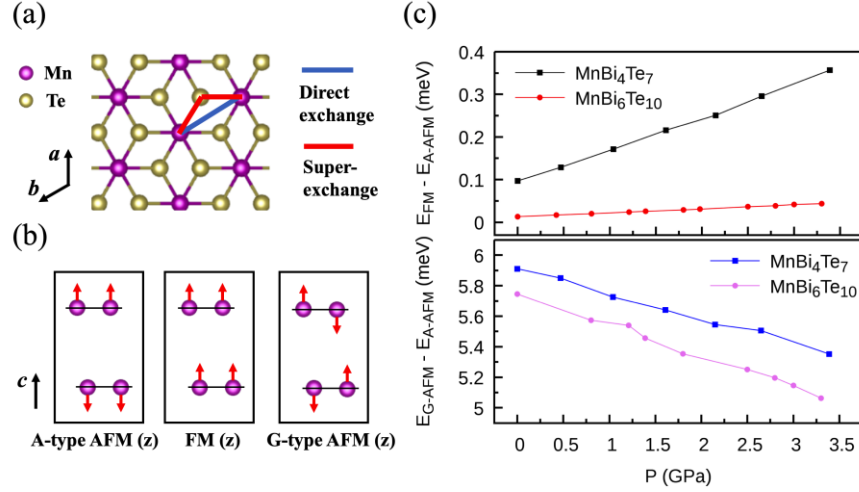


Fig. 3. (a) Schematic of the stacking of Mn and its adjacent Te layers with top view, showing the intralayer exchange coupling within a magnetic layer of MnBi_2Te_4 . The intralayer coupling is determined by the competition of the direct exchange coupling between two adjacent Mn atoms (blue) and the superexchange coupling mediated by Te atoms (red). (b) Schematics of the magnetic configurations for A-AFM, FM and G-AFM phases. The red arrows represent the direction of the magnetic moments. (c) Top panel: the energy difference between FM and A-AFM phases for MnBi_4Te_7 (black square) and $\text{MnBi}_6\text{Te}_{10}$ (red dot) at different pressure; bottom panel: the energy difference between G-AFM and A-AFM phases for MnBi_4Te_7 (blue square) and $\text{MnBi}_6\text{Te}_{10}$ (purple dot) as pressure changes.

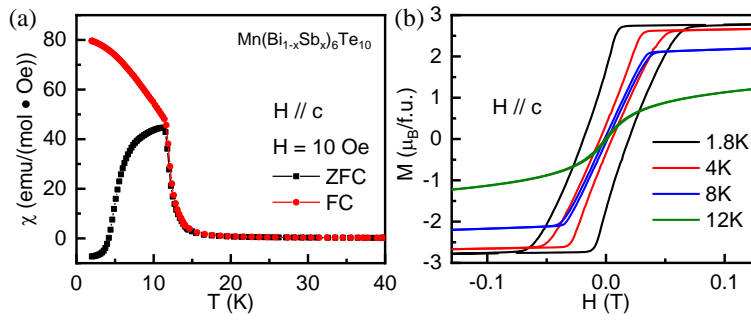


Fig. 4. (a) Temperature dependence of ZFC and FC magnetic susceptibility of Sb doped $\text{MnBi}_6\text{Te}_{10}$ with an applied magnetic field of 10 Oe along c axis. (b) Isothermal magnetization curves of the Sb doped $\text{MnBi}_6\text{Te}_{10}$ below 15K with $H // c$. The FM loop stays clear with no kinks associated with the AFM states up to the magnetic ordering temperature of 11.5K.